

https://doi.org/10.1038/s43246-024-00694-v

# Unraveling the origin of conductivity change in Co-doped FeRh phase transition

Check for updates

Ji-Ho Park<sup>1,7</sup>, Min Tae Park<sup>2,7</sup>, Geon-Woo Baek <sup>1,7</sup>, Shin-ichi Kimura <sup>3,4,5</sup>, Myung-Hwa Jung <sup>2</sup> ≥ & Kab-Jin Kim <sup>1,6</sup> ≥

Phase-changing materials have been a cornerstone of condensed matter physics for decades. A quintessential example is iron-rhodium (FeRh), which undergoes a first-order phase transition from antiferromagnetic to ferromagnetic states near room temperature. The pivotal aspect of this transition is a marked alteration in electrical conductivity. However, its underlying origin still remains elusive, largely due to the difficulties of directly probing fundamental transport during this phase transition. In this study, we investigate the fundamentals of FeRh's electrical transport employing terahertz time-domain spectroscopy (THz-TDS). Leveraging the Drude model, we discerned the distinct contributions of extrinsic (momentum scattering time,  $\tau$ ) and intrinsic (charge density, n, and effective mass, n\*) factors to electrical conductivity independently. Notably, our investigation unveiled a sharp alteration in n and n\* during the phase transition, contrasting with the gradual monotonic decrease of  $\tau$  with rising temperature. Consequently, our findings provide compelling evidence that the conductivity change in FeRh during the phase transition originates from a restructuring of its band structure. This work provides a crucial step towards a comprehensive understanding of the electrical transport changes occurring during the phase transition, offering valuable insights into the behaviour of phase changing materials.

The intermetallic compound FeRh, initially discovered in 1938<sup>1</sup>, has garnered significant attention due to its notable magnetic phase transition from antiferromagnetic (AFM) to ferromagnetic (FM) phases near room temperature. This transition is characterized by a modest 1% expansion of the unit cell<sup>2</sup> and a substantial 50% change in electrical conductivity<sup>3</sup>. Remarkably, the phase transition in FeRh is influenced not only by temperature but also by magnetic fields or doping<sup>4</sup>, making FeRh-based materials attractive for various applications, including heat-mediated antiferromagnetic memory<sup>5,6</sup>, magnetic refrigeration<sup>7,8</sup>, and magnetic sensors<sup>9,10</sup>. Despite extensive research efforts, however, our understanding of the phase transition of FeRh remains incomplete.

A longstanding question pertains to the fundamental origin of the conductivity change during the phase transition of FeRh. The large conductivity change of FeRh has often been likened to the mechanism of giant magnetoresistance (GMR), where conductivity depends on the relative orientation of magnetic layers, parallel or antiparallel. While each atomic layer of FeRh could theoretically be treated as a GMR layer<sup>11</sup>, directly applying the GMR concept—namely, spin-dependent scattering—to FeRh

is not straightforward. This is because the phase transition in FeRh could also accompany the changes in electronic structure, differing from the GMR. Early studies indeed pointed out that the conductivity change of FeRh is due to intrinsic band structure reconstruction during the phase transition, with the formation/disappearance of a superzone gap<sup>12,13</sup>. Specifically, these studies proposed that since the antiferromagnetic state features a periodic alternating spin structure, it introduces a new Brillouin-zone boundary induced by the doubled magnetic lattices. Consequently, the Fermi surface is intersected by the new Brillouin-zone boundaries in the AFM state, leading to an energy gap in the electron dispersion relation and thus a decrease in charge carrier density. However, recent theoretical studies have emphasized that conductivity should depend not only on intrinsic band structure but also on extrinsic scattering<sup>14,15</sup>. These studies argue that the AFM state exhibits more pronounced magnetic disorder compared to the FM state, resulting in a smaller scattering time and hence a higher resistivity in the AFM state. Consequently, there is a need for experimental approaches that can distinguish between intrinsic and extrinsic contributions to the electrical transport of FeRh.

<sup>1</sup>Department of Physics, KAIST, Daejeon, Republic of Korea. <sup>2</sup>Department of Physics, Sogang University, Seoul, Republic of Korea. <sup>3</sup>Graduate School of Frontier Biosciences, Osaka University, Suita, Japan. <sup>4</sup>Department of Physics, Graduate School of Science, Osaka University, Toyonaka, Japan. <sup>5</sup>Institute for Molecular Science, Okazaki, Japan. <sup>6</sup>Graduate School of Quantum Science and Technology, KAIST, Daejeon, Republic of Korea. <sup>7</sup>These authors contributed equally: Ji-Ho Park, Min Tae Park, Geon-Woo Baek. —e-mail: mhjung@sogang.ac.kr; kabjin@kaist.ac.kr

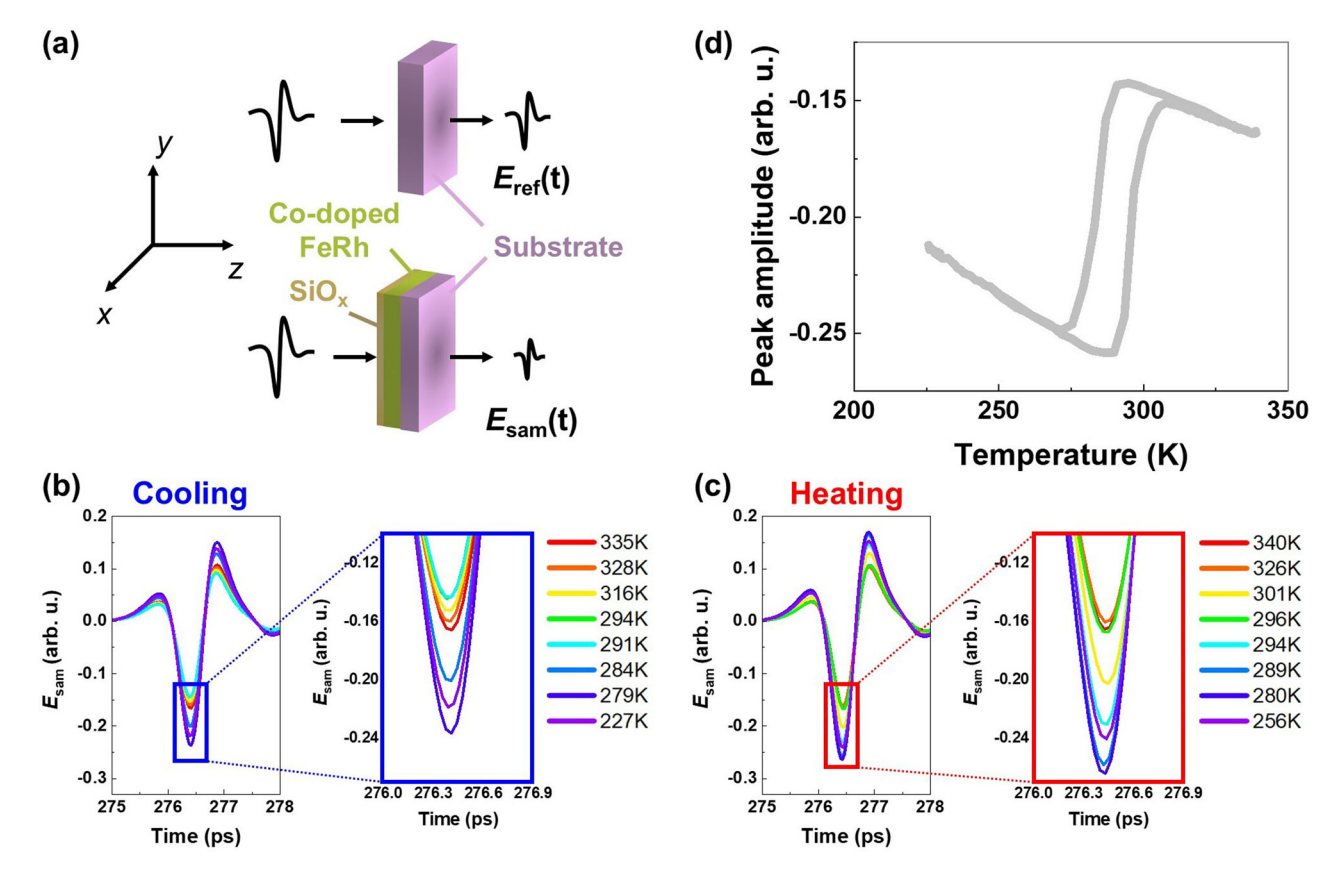


Fig. 1 | Terahertz time domain spectroscopy (THz-TDS) measurement of FeRh across the phase transition temperature. a Schematic illustrations of our THz-TDS absorption experiment (b), (c) Time domain spectra obtained under 8 different temperatures during (b) cooling and (c) heating. Negative pulse peaks are enlarged

in blue and red boxes for cooling and heating, respectively.  $\mathbf{d}$  Temperature-dependent pulse peak amplitude measured by THz measurements. THz spectrums were measured while sweeping the temperature, which slightly differ from  $(\mathbf{b})$  and  $(\mathbf{c})$  where data were obtained at several fixed temperatures.

In this work, we employ THz time-domain spectroscopy (THz-TDS) to independently quantify the extrinsic and intrinsic contributions to the electrical conductivity of FeRh  $^{16-21}$ . Our observations reveal that the extrinsic scattering time ( $\tau$ ) does not exhibit an abrupt change during the phase transition but rather shows a temperature-dependent monotonic decrease. In contrast, the intrinsic contributions (n and  $m^*$ ) undergo a significant change: both n and  $m^*$  experience a pronounced increase as FeRh transitions from AFM to FM phases. This suggests that the conductivity change in FeRh during the phase transition is predominantly due to the intrinsic origin arising from electronic band reconstruction, contrasting with GMR where conductivity change primarily arises from extrinsic electron scattering while the electronic band structure remains unchanged  $^{19}$ . Our results provide experimental evidence for the fundamental origin of the conductivity change in FeRh, underscoring the need for further theoretical investigations to achieve a complete understanding of the phase transition in FeRh.

# Results and Discussion Sample and measurement set-up

For this study, a 73-nm-thick FeRh film was deposited on a MgO substrate and capped with 2 nm  $\rm SiO_x$  by DC magnetron sputtering under the working pressure of 3 mTorr and temperature of 600 °C, followed by annealing at 800 °C for 10 h. Here, we doped a small amount of Co ( ~ 1.51 at.%) into FeRh to match the phase transition temperature due to the limited measurement temperature range in our THz-TDS set-up (16 K ~ 350 K). Detailed investigation regarding the Co doping level is available in Supplementary Note 1. We note that doped Co replaces Rh sites and lowers the phase transition temperature without significantly altering the concentration of valence electrons<sup>4,22</sup>, thereby, essential properties such as crystal structure, saturation magnetic moment, Hall coefficient, and carrier density unaffected.

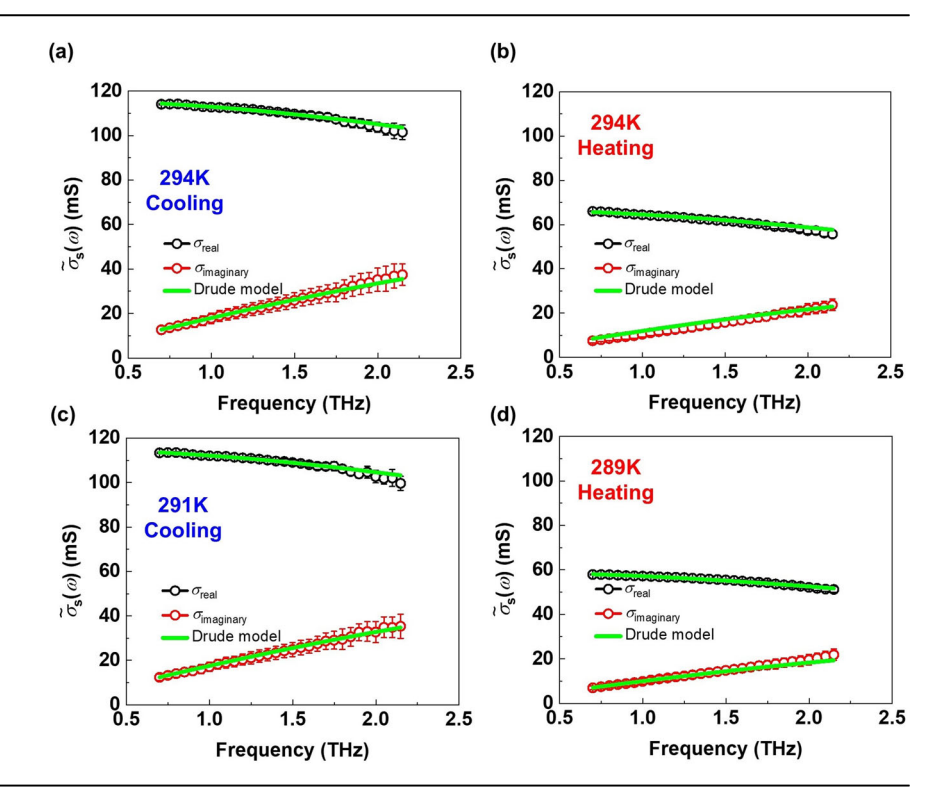
A schematic illustration of our THz-TDS absorption experiment is shown in Fig. 1a. We used a standard THz-TDS set-up, where a weak single-cycle THz pulse with 2 picosecond duration is illuminated normally at the sample, and its transmission is measured (see Methods for detailed setup). As the THz electric field, with an amplitude of ( $E_{\rm THz}$ ) is 100 V/cm, induces an oscillating current in the sample, the attenuation and phase delay of THz electric field was observed as it propagates through the sample. The detected THz pulse was then transformed into the frequency domain by fast Fourier transform (FFT), and the complex conductivity of sample was finally determined from the FFT spectra based on Tinkham formula (see Methods for detailed procedures). We note that the contribution of the THz magnetic field is negligible, as the field strength ( $B_{\rm THz}$ ) is only 0.033 mT (see Supplementary Note 2 for more information).

The experiments were performed by sweeping the temperature in the range of  $T=228\sim342$  K, which is enough to observe the phase transition of our FeRh. Measurements were performed below 1% of relative humidity and under zero magnetic field.

#### **Detection of FeRh phase transition using THz-TDS**

Figure 1b, c display the time-domain pulse data observed at various temperatures during cooling and heating, respectively. Blue and red boxes highlight enlarged negative peaks for cooling and heating, respectively. Notably, the pulse peak amplitudes exhibit substantial variations with temperature changes for both cooling and heating. This suggests significant alterations in the electrical conductivity of FeRh during the phase transition, as higher conductivity leads to greater absorption of the electric field and thus smaller transmitted pulse peak amplitudes. Moreover, the pulse peak amplitudes at the same temperatures differ between cooling and heating, indicating temperature-dependent hysteresis. The variation in pulse peak

Fig. 2 | Complex sheet conductivity of FeRh obtained via THz-TDS during heating and cooling. a 294 K and (c) 291 K during cooling, and (b) 294 K and (d) 289 K during heating. Black and red points correspond to the real and imaginary parts of THz conductivities, respectively. The green lines represent fitting lines based on the Drude model.



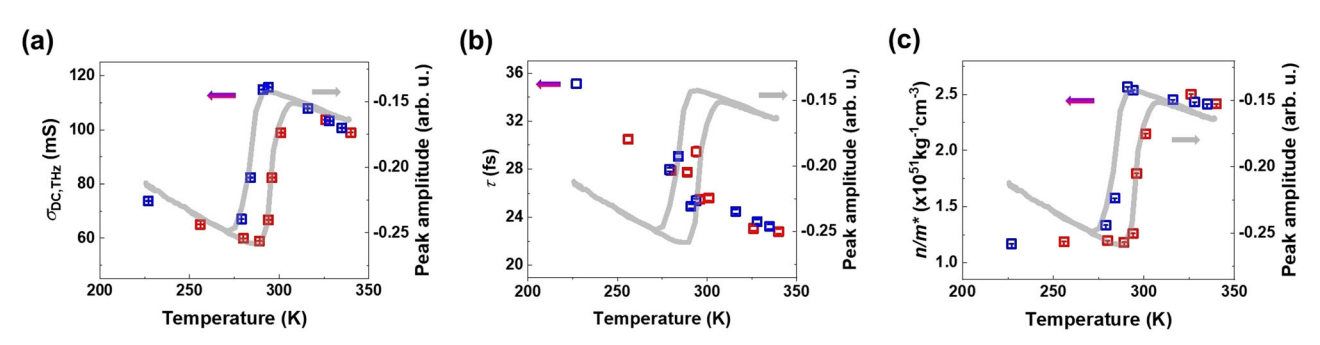


Fig. 3 | Temperature-dependent intrinsic and extrinsic transport parameters probed by THz-TDS. Temperature-dependent negative pulse peak amplitude (gray line) obtained from Fig. 1d, compared with (a) the DC sheet conductivity

 $\operatorname{Re}\left[\widetilde{\sigma}_{S}(0)\right] \equiv \sigma_{DC}\left(\mathbf{b}\right)$  extrinsic contribution,  $\tau$  and  $(\mathbf{c})$  intrinsic contribution,  $n/m^{*}$  obtained by analyzing complex THz conductivity based on the Drude model. Cooling data are represented in blue, while heating data are shown in red.

amplitude is summarized in Fig. 1d, where a pronounced hysteresis is evident with a significant change in pulse amplitude. This confirms that THz measurements accurately capture the phase transition of FeRh.

#### THz conductivity spectra and Drude fitting of FeRh

We performed THz conductivity measurements at 8 different fixed temperatures during both heating and cooling. Figure 2 illustrates representative data of complex THz sheet conductivities measured at similar temperatures (additional temperatures are detailed in Supplementary Notes 3 and 4). In the figure, black and red data points represent the real and imaginary parts of THz conductivities, respectively. The sign of the imaginary part of conductivity is determined by the Fourier transformation convention:  $e^{-i\omega t}$  is multiplied during the conversion from the time domain to the frequency domain. Remarkably, the terahertz conductivity at similar temperatures differs depending on whether it is during cooling or heating, indicating once again the presence of hysteresis in the phase transition. The green lines in Fig. 2 depict the best fits based on the Drude model,

$$\widetilde{\sigma}_{S}(\omega) = \sigma_{real} + \sigma_{ima} = \frac{d \cdot \sigma_{DC}}{1 + \omega^{2} \tau^{2}} + i \frac{d \cdot \sigma_{DC}}{1 + \omega^{2} \tau^{2}} \omega \tau \tag{1}$$

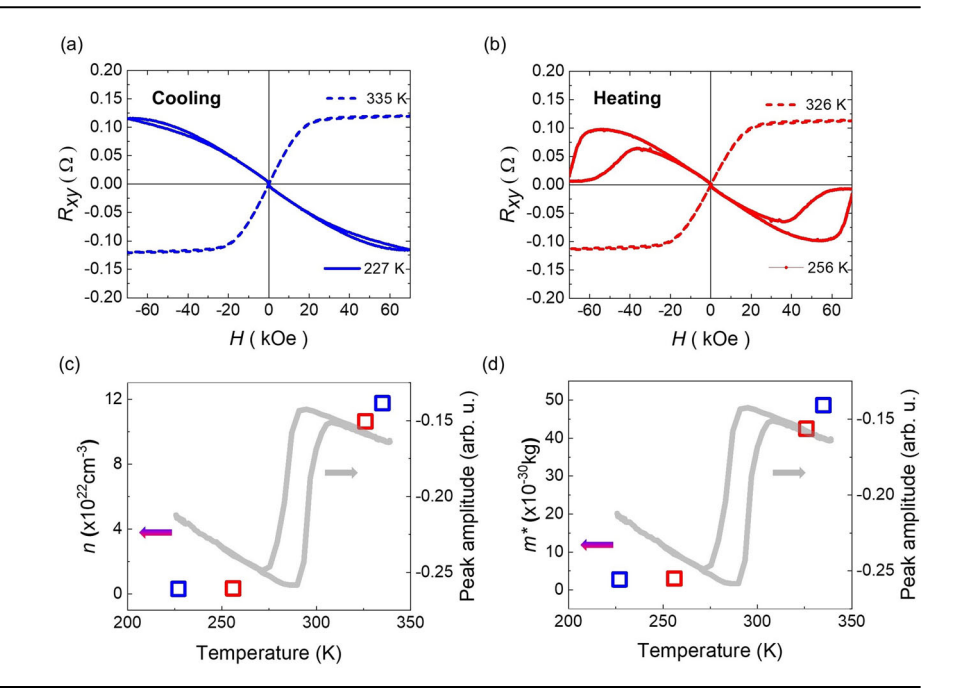
where  $\omega/2\pi (=f)$  is the frequency,  $\tau$  is the momentum scattering time,  $\sigma_{DC}$  is the DC sheet conductivity, and d is the thickness of the film. The fitting results demonstrate that the Drude conduction model effectively describes the measured THz conductivity at all temperatures<sup>19–21</sup>.

# **Analysis of Drude fitting**

THz spectroscopy enables the direct determination of the real and imaginary components of the complex conductivity, thereby allowing for simultaneous extraction of the momentum scattering time  $\tau$  and DC sheet conductivity  $\sigma_{\rm DC}$  based on Eq. (1). Consequently, it can further isolate  $n/m^*$  from the definition of  $\sigma_{DC} = \frac{n}{m^*}e^2\tau$  in the Drude model <sup>19–21</sup>. Figure 3a–c summarize the extracted values from the Drude fitting for several temperatures. These plots are overlaid with the temperature-dependent peak amplitude obtained in Fig. 1d (gray line) to compare the results with the phase transition.

Figure 3a illustrates the DC sheet conductivity,  $\sigma_{DC}$ , obtained by THz measurement. It is clear that the variation of  $\sigma_{DC}$  closely matches the change in the THz peak amplitude, confirming again that THz measurements accurately reflect the phase transition of FeRh. Figure 3b depicts the temperature-dependent variation of  $\tau$ , corresponding to the scattering-dependent extrinsic contribution. Surprisingly,  $\tau$  exhibits neither hysteresis

Fig. 4 | Hall measurements of FeRh across the phase transition temperature. a Hall resistance as a function of magnetic field during cooling for  $T=335~\mathrm{K}$  (FM phase) and  $T=227~\mathrm{K}$  (AFM phase). b Hall resistance as a function of magnetic field during heating for  $T=256~\mathrm{K}$  (AFM phase) and  $T=326~\mathrm{K}$  (FM phase). c Temperature-dependent carrier density, n, obtained from the Hall measurements during cooling (blue) and heating (red). d Temperature-dependent effective mass,  $m^*$ , obtained from the Hall-determined n and THz-determined  $n/m^*$  during cooling (blue) and heating (red).



nor abrupt jump during the phase transition. Instead, the overall temperature dependence of  $\tau$  exhibits a monotonic decrease as the temperature rises. This trend aligns with the typical behavior observed in conventional magnetic metals, where the electron scattering rate increases with temperature due to thermal fluctuation from the influence of phonons and magnons. Consequently, the experimentally determined  $\tau$  implies that the scattering-dependent extrinsic contribution is not the primary origin of the abrupt conductivity change during the phase transition of FeRh.

Figure 3c shows the temperature-dependent change of  $n/m^*$ , representing the scattering-independent intrinsic contribution. In contrast to  $\tau$ ,  $n/m^*$  undergoes a substantial increase during the phase transition with increasing temperature, nearly doubling at the FM state compared to the AFM state. This suggests that the scattering-independent intrinsic contribution is the primary origin of the conductivity change during the phase transition of FeRh. Notably, the value of  $n/m^*$  remains nearly unchanged when the FeRh stays in the AFM or FM states, indicating that the linear decrease in DC conductivity with temperature at either state originates from the change in extrinsic factor  $\tau$ . We note that the high-frequency correction in the Drude fitting due to optical phonons does not affect the trend in  $\tau$  and  $n/m^*$  (see Supplementary Notes 5)<sup>22,23</sup>.

To further isolate the carrier density (n) and effective mass  $(m^*)$ from the ratio  $n/m^*$ , we conducted Hall measurements. Figure 4a, b presents the Hall measurement results during cooling and heating, respectively. We specifically focus on temperatures low and high enough where the AFM and FM phases dominate, as the Hall curve at intermediate temperatures where the AFM and FM phases mix becomes complicated and challenging to analyze. It is evident that the slope of the Hall resistance curve is negative for the AFM state, indicating the dominance of electrons, while it is positive for the FM state, indicating the prevalence of holes, consistent with previous reports<sup>9,13</sup>. The carrier density n is then estimated using the approach descried in Ref. 9. Figure 4c summarizes the carrier density determined from the Hall measurements, revealing an approximately 30-fold increase from AFM phase  $(n_{AFM} = 3.4 \times 10^{21} cm^{-3})$  to FM phase  $(n_{FM} = 1.1 \times 10^{23} cm^{-3})$ . This variation in n aligns with the theory that superzone boundaries in the AFM state lead to an energy gap in electron dispersion relation, resulting in a lower charge carrier density<sup>12</sup>. Further analysis based on the comparison between  $n/m^*$  from Fig. 3c and n from Fig. 4c allows us to quantify  $m^*$ , revealing that the effective mass  $m^*$  is also different between the AFM ( $m_{AFM}^* = 2.8 \times 10^{-30}$ kg) and FM ( $m_{FM}^* = 4.5 \times 10^{-29}$ kg) states. Considering that the effective mass in a solid is inversely proportional to the curvature of the dispersion relation, the low effective mass in the AFM state may suggests a strongly curved dispersion owing to the formation of the superzone in the AFM state, but further theoretical investigation is required to elucidate the fundamental origin of effective mass change.

#### Infrared spectroscopy of FeRh

To further corroborate the variations in intrinsic transport parameters during the phase transition, we conducted infrared (IR) reflectance spectroscopy, which probes electron transport in a higher frequency region than THz spectroscopy. The IR reflectivity spectra were measured at various temperatures across the phase transition. Figure 5a displays representative data of the obtained IR spectra measured at 200 K and 320 K, respectively, where the AFM and FM phases dominate (additional temperatures are detailed in Supplementary Notes 6). As the IR spectrum encompasses both resonance and electron transport phenomena, we employed the Drude-Lorentz model for fitting (see Methods for detailed procedures). The blue solid lines in Fig. 5a depict the fitting curves, allowing us to determine  $n/m^*$ which is summarized in Fig. 5b. The results reveal an approximately 10-fold difference in  $n/m^*$  between AFM and FM states. While this value slightly differs from the THz-TDS result due to the distinct frequency regimes, the significant change in  $n/m^*$  observed in IR spectroscopy supports that the FeRh phase transition is accompanied by a substantial change in the band structure, resulting in the conductivity change.

Lastly, we examined the spectral intensity of the IR spectrum, reflecting the density of states of the electronic structure. Figure 5c illustrates the real part of the optical conductivity spectra  $\sigma_1(\omega)$  of FeRh, revealing a notable enhancement in spectral intensity at high temperatures (FM phase) and suppression at low temperatures (AFM phase). This observation suggests a higher (lower) density of states near the Fermi level in the FM (AFM) state, providing further evidence of band structure reconstruction during the phase transition of FeRh.

#### Conclusions

In this study, we revealed the origin of FeRh conductivity change during its phase transition from antiferromagnet (AFM) to ferromagnet (FM). Leveraging terahertz time-domain spectroscopy (THz-TDS), we acquired the temperature-dependent terahertz conductivity of FeRh, enabling us to discern the intrinsic (carrier density, n, and effective mass,  $m^*$ ) and extrinsic (scattering time,  $\tau$ ) contributions to FeRh conductivity.

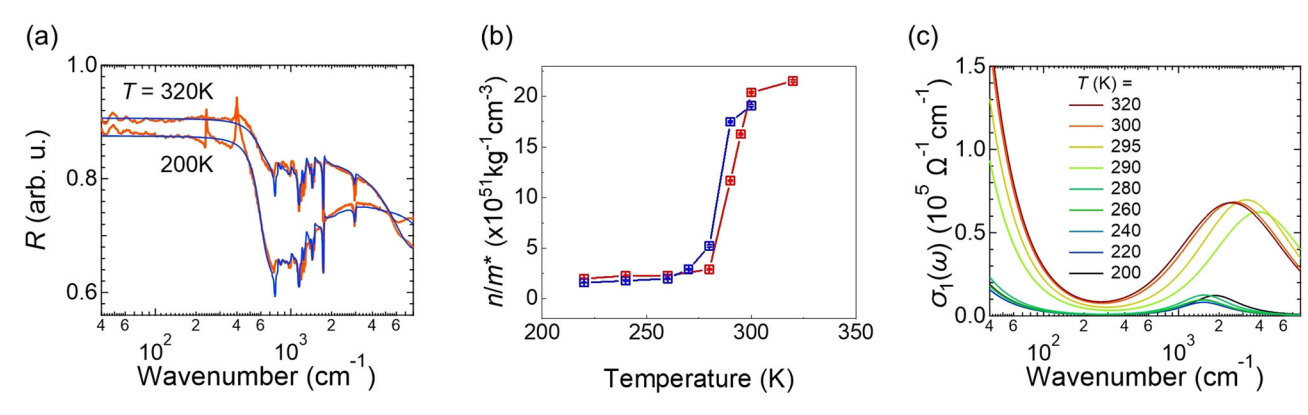


**Fig. 5** | **Infrared spectroscopy of FeRh. a** Infrared (IR) reflectivity spectra at the lowest ( $T = 200 \, \text{K}$ ) and highest ( $T = 320 \, \text{K}$ ) temperatures, respectively. Note that the observed phonon peaks at 250 and 400 cm<sup>-1</sup> are excluded. **b** Temperature-dependent

 $n/m^*$ . **c** Real part of optical conductivity spectra,  $\sigma_1(\omega)$ , of FeRh obtained from the IR spectroscopy.

Our investigation unveiled that the substantial change in electrical conductivity of FeRh primarily stems from intrinsic origins (n and  $m^*$ ) rather than extrinsic factor  $(\tau)$ . Notably, our findings indicate that the carrier density (n) and effective mass  $(m^*)$  of the FM state exceed those of the AFM state by at least one order of magnitude. This underscores the dominance of band structure reconstruction over spin disorder in conductivity change during the phase transition of FeRh. Additionally, our THz-TDS measurements were corroborated by infrared (IR) measurements, lending further credence to our results. By providing the fundamental transport parameters during the phase transition of FeRh, our study underscores the necessity for comprehensive theoretical investigations into FeRh's phase transition dynamics. Furthermore, our work underscores the versatility of THz-TDS as a tool for probing fundamental transport phenomena. Therefore, this work will trigger further theoretical and experimental studies, not only limited to FeRh but also extending to various materials undergoing phase transitions.

#### Methods

# Film growth and characterization

The FeRh films were grown on MgO(001) substrates by conventional dc magnetron sputtering with FeRh alloy target in a base pressure of  $8\times 10^{-7}$  Torr and an Ar process pressure of 3 mTorr. The sputtering power was 130 W and the growth temperature was 600 °C. After deposition, the films were annealed in situ for 10 h at 800 °C, and then cooled down in vacuum. SiO<sub>2</sub> capping layers were deposited on the FeRh films at room temperature. The carrier density in Fig. 4 was determined through Hall measurements using the Van der Pauw method, performed with a physical property measurement system (PPMS).

# Terahertz time domain spectroscopy (THz-TDS)

Montana vacuum cryostat was used to control the temperature of sample. A standard glass windows were replaced with the TPX windows for THz experiment. The deposited film and reference substrate were installed simultaneously inside the cryostat using L-shaped sample holder. Two samples (deposited film and reference substrate) were attached to each plane of L-shaped holder that was attached at the ANC300 piezo rotator. By rotating the piezo rotator, we could selectively choose the deposited film or reference substrate without breaking the vacuum.

A standard THz-TDS setup (Tera K15-Menlosystems) with 4 TPX lenses was used for THz measurement. A single cycle THz pulse with 2 ps duration was generated from the THz emitter and then, the THz beam was focused on sample through the TPX lens. The intensity of THz pulse was about 0.1 kV/cm. The transmitted pulse was collimated and detected at the THz detector. For the frequency analysis, we performed the Fourier transformation from the time domain pulse data.

## Complex conductivity measurement

The determination of complex sheet conductivity involves a multi-step process. Initially, the frequency-dependent amplitude  $A(\omega)$  and phase  $\phi(\omega)$  of electric field  $E(\omega)$  passing through the sample are obtained through Fourier transform. To eliminate background interference, an identical measurement is conducted on a reference substrate. This step is crucial as the imaginary part of THz conductivity is sensitive to phase information. The reference substrate chosen is located adjacent to the substrate used for FeRh deposition, minimizing thickness differences between the two substrates

The obtained amplitudes and phases are then incorporated into the Tinkham equation 19,24

$$\frac{E_{sam}(\omega)}{E_{ref}(\omega)} = \frac{n_{sub} + 1}{n_{sub} + 1 + Z_0 \widetilde{\sigma}_s(\omega)}$$
(2)

where  $Z_0$  is the vacuum impedance and  $n_{sub}$  is the refractive index of substrate. We note that the Tinkham's approach is valid in our system, as the internal multiple reflection signals do not get weaker by a skin depth of FeRh at THz frequencies. By inserting the experimentally obtained  $E_{sam}(\omega) = A(\omega)e^{i\phi(\omega)}$  and  $E_{ref}(\omega) = A_{ref}(\omega)e^{i\phi_{ref}(\omega)}$  into Eq. (2), the complex conductivity can be determined as

$$\widetilde{\sigma}_{s}(\omega) = \left[ \left( \frac{A_{\text{ref}}(\omega)e^{i\phi_{\text{ref}}(\omega)}}{A(\omega)e^{i\phi(\omega)}} \right) - 1 \right] * \frac{\left[ n_{\text{sub}} + 1 \right]}{Z_{0}} \\
= \left[ \left\{ \frac{A_{\text{ref}}(\omega)}{A(\omega)} \cos(\phi_{\text{ref}}(\omega) - \phi(\omega)) - 1 \right\} \right. \\
\left. + i \left\{ \frac{A_{\text{ref}}(\omega)}{A(\omega)} \sin(\phi_{\text{ref}}(\omega) - \phi(\omega)) \right\} \right] * \frac{\left[ n_{\text{sub}} + 1 \right]}{Z_{0}}$$
(3)

This process gives both the real and imaginary parts of complex sheet conductivity  $\widetilde{\sigma}_s(\omega)$ . Here, the refractive index of the substrate  $n_{sub}$ , which depends on frequency, is determined through an independent experiment, following Ref. 25. We confirmed that the obtained  $n_{sub}$  is consistent with previous results<sup>26</sup>. Once the real and imaginary conductivities were obtained, the scattering time and DC conductivity can be directly determined by using Drude model. The error bars for AC conductivity represent the standard deviation of the measurements, calculated from the average of 50 data points taken at each temperature. The error bars for  $\tau$  and other extracted parameters were determined by the fitting errors that occur when applying the Drude model to AC conductivity data obtained from THz-TDS measurements.

#### Details of IR measurement

To obtain the optical constants of FeRh, we have assumed the optical spectrum due to the electronic structure consisting of the sum of a Drude- and a Lorentz-functions, and the parameters change with temperature. Based on the assumption, the complex dielectric function  $\tilde{\epsilon}(\omega)$  of FeRh can be written as

$$\tilde{\varepsilon}(r) = \varepsilon_{\infty} - \frac{ne^2}{m^*} \frac{1}{\omega(1+i\gamma)} + \frac{\Omega_p^2}{(\Omega_0^2 - \omega^2) - i\Gamma\omega}$$
 (4)

and the complex refractive index  $\widetilde{n}(\omega)$  is  $\widetilde{n}(\omega) = \sqrt{\widetilde{\epsilon}(\omega)}$  where  $\varepsilon_{\infty}$  is the dielectric constant due to interband transitions in the higher energy region, n, e,  $m^*$ , and  $\gamma$  are the carrier density, the electron charge, the effective mass of an electron, and the damping constant of carriers, respectively,  $\Omega_{\rm p}$ ,  $\Omega_{\rm 0}$  and  $\Gamma$  are the plasma frequency, the resonant frequency, and the damping constant, respectively, of the interband transition.

# **Data availability**

The data supporting the findings of this study are included in the paper and its Supplementary Materials file. Further data sets are available from the corresponding author on reasonable request.

Received: 8 May 2024; Accepted: 4 November 2024; Published online: 11 November 2024

#### References

- Fallot, M. & Hocart, R. Sur l'apparition du ferromagnétisme par élévation de température dans des alliages de fer et de rhodium. Rev. Sci. 77, 498 (1939).
- Ibarra, M. R. & Algarabel, P. A. Giant volume magnetostriction in the FeRh alloy. *Phys. Rev. B* 50, 4196–4199 (1994).
- Suzuki, I., Naito, T., Itoh, M., Sato, T. & Taniyama, T. Clear correspondence between magnetoresistance and magnetization of epitaxially grown ordered FeRh thin films. J. Appl. Phys. 109, 07C717 (2011).
- Barua, R., Jiménez-Villacorta, F. & Lewis, L. H. Predicting magnetostructural trends in FeRh-based ternary systems. *Appl. Phys. Lett.* 103, 102407 (2013).
- Marti, X. et al. Room-temperature antiferromagnetic memory resistor. Nat. Mater. 13, 367–374 (2014).
- Moriyama, T. et al. Sequential write-read operations in FeRh antiferromagnetic memory. Appl. Phys. Lett. 107, 122403 (2015).
- Annaorazov, M. P. et al. Anomalously high entropy change in FeRh alloy. *J. Appl. Phys.* 79, 1689–1695 (1996).
- Pecharsky, V. K. et al. Thermodynamics of the magnetocaloric effect. *Phys. Rev. B.* 64, 144406 (2001).
- 9. De Vries, M. A. et al. Hall-effect characterization of the metamagnetic transition in FeRh. *New. J. Phys.* **15**, 013008 (2013).
- Pecharsky, V. K. et al. Making the most of the magnetic and lattice entropy changes. J. Magn. Magn. Mater. 321, 3541–3547 (2009).
- 11. Moruzzi, V. L. & Marcus, P. M. Giant magnetoresistance in FeRh: a natural magnetic multilayer. *Phys. Rev. B* **46**, 14198 (1992).
- Baranov, N. V. & Barabanova, E. A. Electrical resistivity and magnetic phase transitions in modified FeRh compounds. *J. Alloy. Compd.* 219, 139–148 (1995).
- Kobayashi, Y., Muta, K. & Asai, K. The Hall effect and thermoelectric power correlated with the giant magnetoresistance in modified FeRh compounds. J. Phys.: Condens. Matter 13, 3335 (2001).
- Kudrnovský, J., Drchal, V. & Turek, I. Physical properties of FeRh alloys: the antiferromagnetic to ferromagnetic transition. *Phys. Rev. B.* 91, 014435 (2015).
- Mankovsky, S. et al. Temperature-dependent transport properties of FeRh. Phys. Rev. B 95, 155139 (2017).
- Taschin, A., Bartolini, P., Tasseva, J. & Torre, R. THz time-domain spectroscopic investigations of thin films. *Measurement* 118, 282–288 (2018).

- Walther, M. et al. Terahertz conductivity of thin gold films at the metalinsulator percolation transition. *Phys. Rev. B* 76, 125408 (2007).
- Cocker, T. L. et al. Terahertz conductivity of the metal-insulator transition in a nanogranular VO2 film. Appl. Phys. Lett. 97, 221905 (2010)
- Jin, Z. et al. Accessing the fundamentals of magnetotransport in metals with terahertz probes. *Nat. Phys.* 11, 761–766 (2015).
- Nádvorník, L. et al. Broadband terahertz probes of anisotropic magnetoresistance disentangle extrinsic and intrinsic contributions. *Phys. Rev. X* 11, 021030 (2021).
- Park, J. H. et al. Temperature dependence of intrinsic and extrinsic contributions to anisotropic magnetoresistance. Sci. Rep. 11, 20884 (2021).
- Wu, L. et al. A sudden collapse in the transport lifetime across the topological phase transition in (Bi<sub>1-x</sub>In<sub>x</sub>)<sub>2</sub>Se<sub>3</sub>. Nat. Phys. 9, 410–414 (2013).
- 23. Lv, Y. et al. Ultrafast THz emission spectroscopy of spin currents in the metamagnet FeRh. *APL Mater.* **12**, 041121 (2024).
- Yuasa, S., Otani, Y., Miyajima, H. & Sakuma, A. Magnetic Properties of bcc FeRh<sub>1-x</sub>M<sub>x</sub> Systems. *IEEE Trans. J. Magn. Jpn.* 9, 202–209 (1994).
- 25. Jepsen, P. U. & Fischer, B. M. Dynamic range in terahertz time-domain transmission and reflection spectroscopy. *Opt. Lett.* **30**, 29–31 (2005).
- Nenno, D. M. et al. Modification of spintronic terahertz emitter performance through defect engineering. Sci. Rep. 9, 13348 (2019).

## **Acknowledgements**

This research was supported by the National Research Foundation of Korea (NRF) funded by the Korean Government (MSIP) [grant numbers: RS-2023-00275259, RS-2023-0027732, 2020R1A2C3008044, 2022R1A4A1033562], and by Samsung Electronics Co., Ltd. (202470076.08). This work was partly supported by the Technology Innovation Program (or Industrial Strategic Technology Development Program) (20020286) funded by the Ministry of Trade, Industry and Energy (MOTIE, Korea), KSRC (Korea Semiconductor Research Consortium) support program for the development of the future semiconductor device; the Samsung Research Funding Center of Samsung Electronics under Project No. SRFC-MA2002-02.

#### **Author contributions**

M.-H.J. and K.-J.K. supervised the project. J.-H.P. and G.-W.B. performed the experiment and analyzed the data. M.T.P. prepared the Co-doped FeRh films and performed the Hall measurement. S.i. K. performed the IR measurement and analyzed it. J.-H.P., M.T.P., G.-W.B. M.-H.J. and K.-J.K. wrote the manuscript. All authors commented and suggested proper modification on manuscript.

# Competing interests

The authors declare no competing interests.

#### **Additional information**

**Supplementary information** The online version contains supplementary material available at https://doi.org/10.1038/s43246-024-00694-y.

 $\begin{tabular}{ll} \textbf{Correspondence} and requests for materials should be addressed to Myung-Hwa Jung or Kab-Jin Kim. \end{tabular}$ 

**Peer review information** *Communications materials* thanks the anonymous reviewers for their contribution to the peer review of this work. Primary Handling Editor: Aldo Isidori. A peer review file is available.

Reprints and permissions information is available at http://www.nature.com/reprints

**Publisher's note** Springer Nature remains neutral with regard to jurisdictional claims in published maps and institutional affiliations.

Open Access This article is licensed under a Creative Commons Attribution-NonCommercial-NoDerivatives 4.0 International License, which permits any non-commercial use, sharing, distribution and reproduction in any medium or format, as long as you give appropriate credit to the original author(s) and the source, provide a link to the Creative Commons licence, and indicate if you modified the licensed material. You do not have permission under this licence to share adapted material derived from this article or parts of it. The images or other third party material in this article are included in the article's Creative Commons licence, unless indicated otherwise in a credit line to the material. If material is not included in the article's Creative Commons licence and your intended use is not permitted by statutory regulation or exceeds the permitted use, you will need to obtain permission directly from the copyright holder. To view a copy of this licence, visit <a href="https://creativecommons.org/licenses/by-nc-nd/4.0/">https://creativecommons.org/licenses/by-nc-nd/4.0/</a>.

© The Author(s) 2024